ACS APPLIED MATERIALS & INTERFACES

Research Article

www.acsami.org

Ordered Assembly of $NiCo_2O_4$ Multiple Hierarchical Structures for High-Performance Pseudocapacitors

Qingwen Zhou,[†] Jiachao Xing,[‡] Yanfang Gao,*[,†] Xiaojun Lv,[§] Yongmei He,[†] Zihan Guo,[†] and Yueming Li*[,∥]

[†]College of Chemical Engineering, Inner Mongolia University of Technology, Hohhot, 010051, People's Republic of China

[‡]State Key Laboratory of Explosion Science and Technology, Beijing Institute of Technology, Beijing, 100081, People's Republic of China

[§]Key Laboratory of Photochemical Conversion and Optoelectronic Materials, CAS and HKU Joint Laboratory on New Materials, Technical Institute of Physics and Chemistry, Chinese Academy of Sciences, Beijing, 100190, People's Republic of China

[∥]State Key Laboratory of Metastable Materials Science and Technology, College of Materials Science and Engineering, Yanshan University, Qinhuangdao, 066004, People's Republic of China

S *Supporting Information*

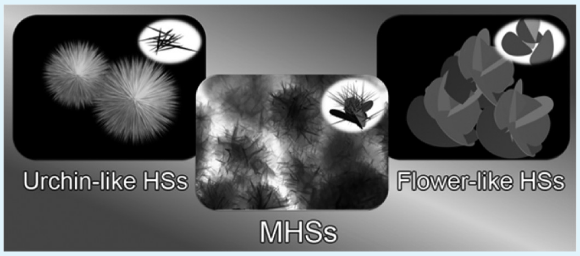

ABSTRACT: The design and development of nanomaterials has become central to the advancement of pseudocapacitive performance. Many one-dimensional nanostructures (1D NSs), two-dimensional nanostructures (2D NSs), and three-dimensional hierarchical structures (3D HSs) composed of these building blocks have been synthesized as pseudocapacitive materials via different methods. However, due to the unclear assembly mechanism of these NSs, reports of HSs simultaneously assembled from two or more types of NSs are rare. In this article, $NiCo_2O_4$ multiple hierarchical structures (MHSs) composed of 1D nanowires and 2D nanosheets are simply grown on Ni foam using an ordered two-step hydrothermal synthesis followed by annealing processing. The low-dimensional nanowire is found to hold priority in the growth order, rather than the high-dimensional nanosheet, thus effectively promoting the integration of these different NSs in the assembly of the $NiCo_2O_4$ MHSs. With vast electroactive surface area and favorable mesoporous architecture, the $NiCo_2O_4$ MHSs exhibit a high specific capacitance of up to 2623.3 F g^{-1}, scaled to the active mass of the $NiCo_2O_4$ sample at a current density of 1 A g^{-1}. A nearly constant rate performance of 68% is achieved at a current density ranging from 1 to 40 A g^{-1}, and the sample retains approximately 94% of its maximum capacitance even after 3000 continuous charge−discharge cycles at a consistently high current density of 10 A g^{-1}.

KEYWORDS: *spinel nickel cobaltate, nickel foam, binder-free electrode, hydrothermal synthesis, hierarchical structure, supercapacitor*

1. INTRODUCTION

Supercapacitors are becoming a new force in the field of electrical energy storage because of their ultrahigh power density, capacity for fast charge−discharge, and durability.[1−5] Those concurrently possessing enhanced energy density and rate performance may be comparable with Li ion batteries, fuel cells, and other power supplies. In theory, the fast multielectron Faradaic redox reaction of pseudocapacitors predicts a much higher specific capacitance (and thus higher energy density) than that observed in double-layer capacitors, whose capacitance mainly results from the electrostatic adsorption of ions at the electrode/electrolyte interface.[6−8] Many different electrode materials have been studied for use in pseudocapacitors, including metal oxides[4,9] and metal sulfides;[10,11] the capacitive properties of the categories vary greatly because of their different pseudocapacitive natures. Moreover, the capacitive performance of each category is affected by the size, morphology, and electrode preparation methods, which also differ widely across the categories.[12] For example, at very high rates, the diffusion channels of those electrode materials without suitable pore architectures may collapse, badly weakening the rate capability and limiting the potential applications.[13,14] Consequently, whether through the selection and preparation of novel electrode materials or by the design of novel microstructures/nanostructures (MSs/NSs), many efforts have been devoted to improving the performance of pseudocapacitors in binder-bearing and binder-free electrode systems.

The spinel $NiCo_2O_4$, a binary oxide, is currently popular as an electrode material due to its outstanding electronic conductivity, multiple convertible valence states, and easily controllable morphologies.[15−17] To date, the different syntheses of one-dimensional (1D) nanowires,[18,19] two-dimensional (2D) nanosheets,[17,20] and three-dimensional (3D)

Received: April 1, 2014
Accepted: July 4, 2014
Published: July 4, 2014

hierarchical structures (HSs)[16,21] composed of nanowires and nanosheets have demonstrated superior capacitive properties compared with some other single-component and multicomponent metal oxides, including even the noble metal oxide RuO_2. One-dimensional $NiCo_2O_4$ nanowires provide short transport pathways for electrons and ions, improving the kinetics of diffusion and facilitating the rate capability in return.[18] Two-dimensional $NiCo_2O_4$ nanosheets, with two dimensions outside the nanometric size range, tend to cross-link with each other. Thus, the large, opened "V-type" space is formed, which serves as a robust reservoir for ions and provides numerous electroactive sites for redox reactions as a result of its very high surface area.[17,22] A 3D HS that is formed from these nanoscale structural units would inherit the above-mentioned advantages while also providing additional benefits, such as improved stability, uniform porosity, and resistance to aggregation.[23,24] Urchinlike and flowerlike $NiCo_2O_4$ HSs are most often reported;[21,24−26] these are composed of nanowires and nanosheets, respectively, in a one-pot synthesis. However, due to the unclear assembly mechanism of these NSs, there has been a gap in the study of multiple hierarchical structures (MHSs) composed of two or more types of NSs (e.g., nanoparticles, nanowires, and nanosheets). It is anticipated that in such a MHS, the high-dimensional NSs could provide the "backbone" mechanical strength and enough attachment points for the low-dimensional NSs, thus allowing the latter to fill around the former ones. More significantly, these MHSs could improve the "composite system" by combining or even magnifying the advantages of each component.

This work represents the first reported synthesis of the $NiCo_2O_4$ MHS (denoted as NCO2), which is constructed of 1D nanowires and 2D nanosheets in a two-step hydrothermal growth process followed by a postannealing treatment. To investigate the assembly mechanism of the $NiCo_2O_4$ MHS, a one-step hydrothermal process and an order-transposed, two-step hydrothermal process were also conducted to synthesize the $NiCo_2O_4$ samples (denoted as NCO1 and NCO3, respectively). For the binder-free electrode, nickel foam was used as substrate for the in situ growth. The current-carrying capability was enhanced through an appropriate tableting process. Intriguingly, the series of investigations demonstrate that the successful production of this MHS largely depends on the order of hydrothermal steps, during which the 2D nanosheets tend to be embraced by 1D nanowires. Due to its unique structure, the $NiCo_2O_4$ MHS yields a high initial discharge capacity of 2623.3 F g^{-1}, which remains as high as 1785.5 F g^{-1} for a 40-fold-enlarged current density and displays excellent cycling performance (1993 F g^{-1} at 10 A g^{-1} after 3000 cycles). More importantly, our present work further extends the research on hierarchical structures and may shed some light on the design of advanced energy materials.

2. EXPERIMENTAL SECTION

Materials Preparation. All reagents were of analytical grade and used as received without further purification. The nickel foam (1 cm × 1 cm) was cleaned by sequential sonication in acetone, 6 M HCl, deionized (DI) water, and absolute ethanol for 20 min each. Our approach for fabricating $NiCo_2O_4$ MHSs on nickel foam substrate as pseudocapacitive electrode involves two key steps, as shown in Scheme 1. In the first hydrothermal process, 2.883 g of urea, 0.951 g of $NiCl_2 \cdot 6H_2O$, and 1.903 g of $CoCl_2 \cdot 6H_2O$ were dissolved in 75 mL of DI water with constant stirring for 30 min. After a piece of the pretreated nickel foam was added, the solution was ultrasonically agitated for another 30 min, sealed in a 100 mL, Teflon-lined, stainless autoclave, and maintained at 120 °C for 7 h. After cooling to room temperature naturally, the sample was cleaned by ultrasonication in both DI water and absolute ethanol for 5 min each, vacuum-dried at 80 °C for 6 h, and annealed at 350 °C in a muffle furnace for 3 h. The obtained product is referred to as NCO1.

Scheme 1. Schematic Illustration of the Two-Step Hydrothermal Synthesis of $NiCo_2O_4$ MHSs on Nickel Foam Substrate

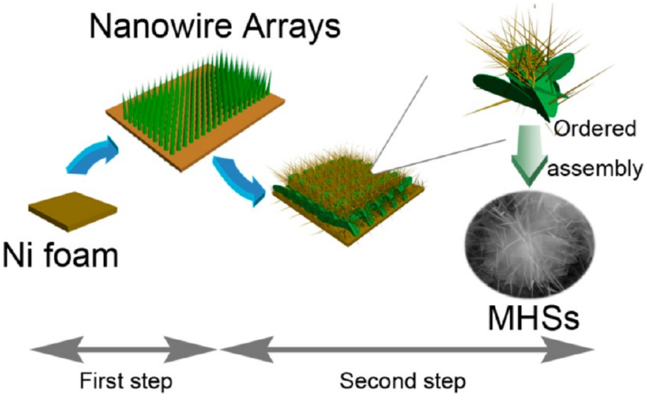

In the second hydrothermal process, the nickel foam covered with the as-grown precursor of NCO1 was considered the substrate and boiled at 120 °C for 7 h in a mixed solution with 25 mL of DI water and 50 mL of ethanol, 1.442 g of urea, 0.476 g of $NiCl_2 \cdot 6H_2O$, and 0.952 g of $CoCl_2 \cdot 6H_2O$. After undergoing the vacuum-drying and thermal treatment described above, the product resulting from the NCO1 precursor was considered to be transformed into the $NiCo_2O_4$ MHS and is referred to as NCO2.

The production of NCO3 was accomplished by merely switching the order of the hydrothermal processes: the product of the "second hydrothermal process", conducted on the cleaned nickel foam, was then used in the "first hydrothermal process" to complete the synthesis of the NCO3. The $NiCo_2O_4$ loadings on nickel foam were 1.22, 2.09, and 2.31 mg cm^{-2} for NCO1, NCO2, and NCO3, respectively. For a direct comparison of the prepared samples to the pure nickel foam electrodes, the pretreated nickel foams (1 cm × 1 cm) were subjected to the same conditions as the prepared samples, with the notable absence of the cobalt and nickel sources.

Material Characterizations. The structures of the products were examined via X-ray diffraction (XRD; Bruker, D8-Advance) using Cu Kα radiation (λ = 1.5406 Å). The morphologies of the samples were characterized by scanning electron microscopy (SEM; Hitachi, S-3400N), field-emission scanning electron microscopy (FESEM; FEI, Quanta 650), and transmission electron microscopy (TEM; JEOL, JEM-2100F). Elemental composition analyses of the products were performed using an energy dispersive X-ray (EDX) attachment. The surface area and pore size distribution analyses were conducted using the Brunauer−Emmett−Teller (BET) method and the Barrett−Joyner−Halenda (BJH) method (Quantachrome, Quadrasorb SI), respectively.

Electrochemical Measurements. Cyclic voltammetry (CV) and electrochemical impedance spectroscopy (EIS) measurements were performed using a potentiostat/galvanostat (Ametek, PAR 2273). EIS tests were performed within a frequency range of 0.01−105 Hz at amplitude of 5 mV versus the open circuit potential. The galvanostatic charge−discharge (CD) measurements were conducted on an electrochemical analyzer (Chenhua, CHI 660C). All experiments were investigated in a three-compartment cell containing 3 M KOH aqueous solution as the electrolyte. The nickel foam (1 cm × 1 cm) coated with electroactive materials was pressed at 10 MPa for 60 s and used as the working electrode. An Hg/HgO electrode was used as the reference electrode, and a piece of platinum net was employed as the counter electrode. To minimize the errors due to an *iR* drop in the electrolyte, the reference electrode was connected to the cell via a double salt bridge system and a Luggin capillary.[27,28] After cell assembly, the working electrode was impregnated within the electrolyte for 2 h under vacuum conditions to ensure that the electrode was wetted thoroughly.

3. RESULTS AND DISCUSSION

The formation mechanism of the $NiCo_2O_4$ samples is explained as follows: the decomposition and hydrolysis of urea during the hydrothermal synthesis lead to the release of OH^- and CO_3^{2-} ions. The generated ions then interact with metal ions, which results in the precipitation of metal carbonate hydroxide. With the annealing treatment, metal carbonate hydroxide salts were decomposed into metal oxides, accompanied by the release of gaseous CO_2 and H_2O. The involved chemical reactions are represented in eqs 1−5:[25]

$$CO(NH_2)_2 + H_2O \rightarrow 2NH_3 + CO_2 \quad (1)$$

$$CO_2 + H_2O \rightarrow CO_3^{2-} + 2H^+ \quad (2)$$

$$NH_3 \cdot H_2O \rightarrow NH_4^+ + OH^- \quad (3)$$

$$2(Co^{2+}, Ni^{2+}) + CO_3^{2-} + 2OH^- + nH_2O \rightarrow (Co, Ni)_2CO_3(OH)_2 \cdot nH_2O \quad (4)$$

$$(Co, Ni)_2CO_3(OH)_2 \cdot nH_2O \xrightarrow{\Delta} NiCo_2O_4 + H_2O + CO_2 \quad (5)$$

The phase purity of the as-prepared samples (NCO1, NCO2, and NCO3), supported on nickel foam, was characterized using XRD, as shown in Figure 1. Except for the three typical peaks derived from the nickel foam substrate, all of the samples obtained by thermal decomposition of the precursors show an X-ray diffraction pattern corresponding to the cubic lattice of the $Fd3m$ space group of the $NiCo_2O_4$ spinel structure (JCPDS Card No. 73-1702, a = 8.114 Å). The EDX elemental composition and quantitative analyses of the three samples (Supporting Information, Figures S1−S3) confirm the predominant chemical constituents and stoichiometric ratio of Ni, Co, and O, which corroborates the XRD studies. The XRD patterns of the pure nickel foam electrodes indicate no chemical change of metal nickel after the hydrothermal syntheses and annealing (Supporting Information, Figure S4). The overall morphologies of the $NiCo_2O_4$ samples were then observed using SEM and FESEM. After the first hydrothermal process and the following annealing treatment, the $NiCo_2O_4$ nanowires (NCO1) uniformly cover the substrate (Supporting Information, Figure S5). The final product of one of the two-step strategies, namely the $NiCo_2O_4$ MHS (NCO2), is vividly depicted in FESEM images. As observed, the MHS is tightly grown against the nickel foam, without leaving uncovered nickel foam (Figure 2a and Figure S6 in the Supporting Information). At high magnification, the MHS is analogous to an assembly of microspheres with diameters of approximately 4−6 μm (Figure 2b,c). These microspheres all possess a 3D architecture, in which the 2D nanosheets run through the whole while the 1D nanowires encircle the nanosheet backbone. Further information about the $NiCo_2O_4$ MHS is obtained from TEM images. Figure 2d shows the features of an individual nanosheet that was exfoliated after intense ultrasonication. Many 1D nanowires are distributed in multiple orientations around the 2D nanosheet, which agrees with the SEM images. The integration of the two NSs is more distinct in Figure 2e. Figure 2f shows the corresponding high-resolution TEM (HRTEM) image of the nanosheet (shown in lighter color in Figure 2e). The clearly revealed lattice fringes with interplanar distances of ~0.47 and ~0.29 nm correspond to the (111) and (220) planes of spinel-structured $NiCo_2O_4$, respectively. Figure 2g shows a higher magnification TEM image of the nanowire (shown in darker color in Figure 2e), which is a porous structure with an estimated diameter of 50−100 nm. An HRTEM image of the nanowire tip is presented in Figure 2h. The corresponding lattice fringes can be well indexed to the (311) crystal faces with d-spacing values of ~0.25 nm. Additionally, the clear diffraction spot array in the selected area electron diffraction (SAED) pattern (Figure 2i) indicates the polycrystalline features of NCO2.[29] The diffraction rings can be assigned to the (111), (220), (311), (222), (400), and (422) planes of the spinel-structured $NiCo_2O_4$, which is in agreement with the XRD analyses.

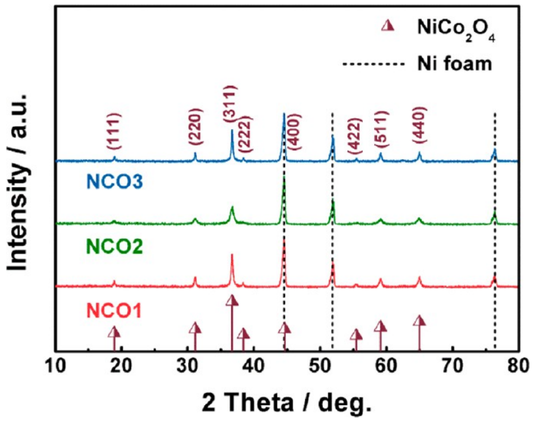

Figure 1. XRD spectra of as-prepared samples on Ni foam and the standard pattern of cubic $NiCo_2O_4$ (JCPDS Card No. 73-1702).

To investigate the formation process of the 3D $NiCo_2O_4$ MHSs, a series of time-dependent experiments were performed during the second hydrothermal growth step. The morphology of the precursor was monitored by FESEM, which showed that the nanowire precursor of NCO1 was grown directly on the smooth surface of the nickel foam (Supporting Information, Figure S7). The formation of these nanowire arrays arises from heterogeneous nucleation and growth via the hydrolysis of urea in aqueous solution, which lowers the interfacial nucleation energy on the substrate. Moreover, the nanowires are interconnected, forming numerous pore paths and open spaces for the permeation and recrystallization of solute during the next hydrothermal growth phase. Observation continued as the substrate began the next hydrothermal growth process. When the reaction was quenched after 1 h, some nubby or sheet-type structures were found to nucleate and form an uneven layer among the interspaces between the nanowires (Figure 3a,b). When the reaction time was increased to 3 h, many nanosheets were discovered in the beginnings of formation and drilling out from the nanowire arrays (Figure 3c,d). The nanosheets also seemed to possess a "winding effect" on the nanowires, impelling the latter to encircle the former. Further increasing the reaction time to 5 h revealed the continued growth of the nanosheets and the formation of connections, tending toward the microspheres. As a consequence, the nanowires became dense and melted into one with the nanosheets (Figure 3e,f). Eventually, with constant growth, the microspheres became increasingly plump and finally formed into MHSs. In contrast

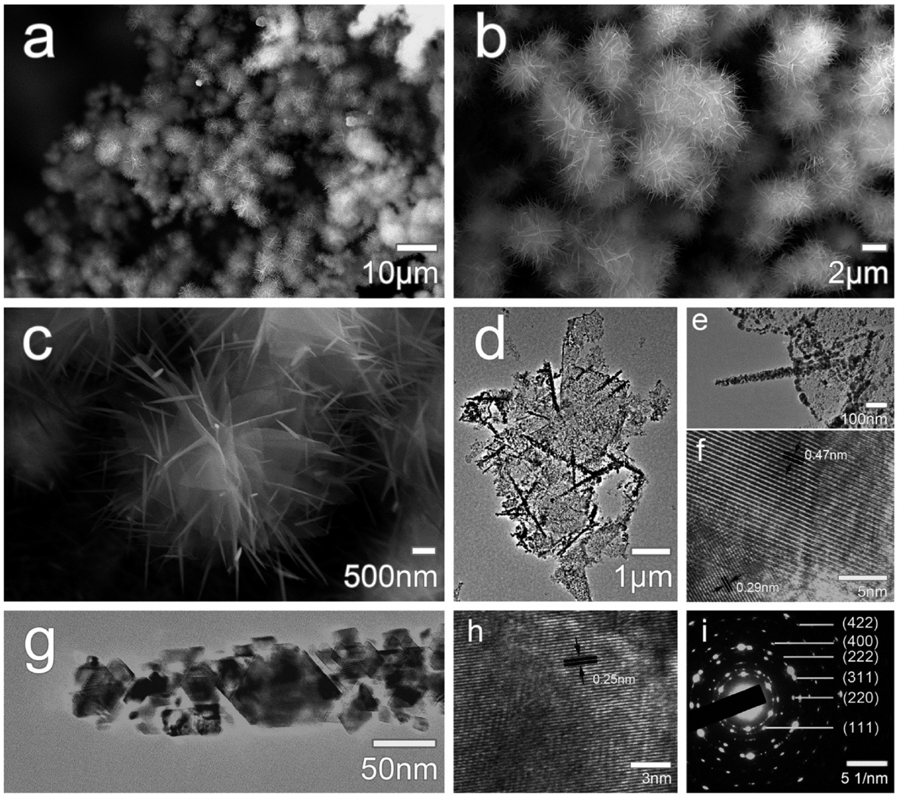

Figure 2. (a−c) FESEM images at different magnifications of $NiCo_2O_4$ MHSs (NCO2) on Ni foam; (d−h) TEM and HRTEM images of the nanosheet and nanowire exfoliated after intense ultrasonication; (i) corresponding SAED pattern of the nanosheet and nanowire.

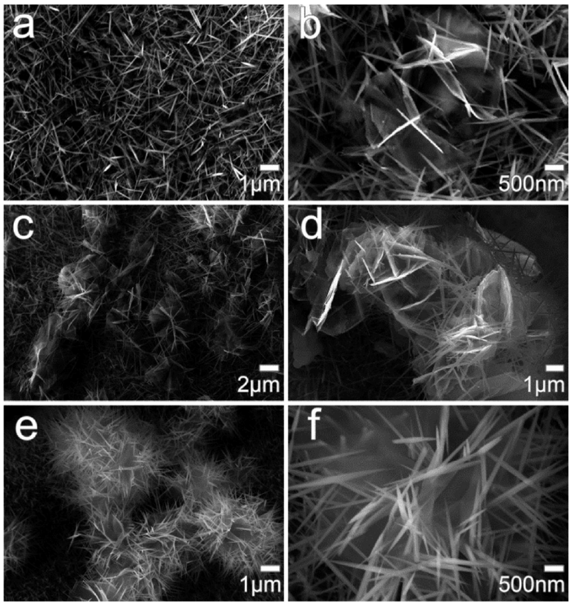

Figure 3. FESEM images of Ni−Co-based intermediate obtained after the second hydrothermal growth with different reaction times: (a, b) 1, (c, d) 3, and (e, f) 5 h.

to the above results, a new two-step strategy, consisting of a reversal of the order of the hydrothermal processes, was also conducted to prove that the formation of the $NiCo_2O_4$ MHS closely relies on the growth sequence of the different NSs. The morphology of the final product (NCO3) was analyzed using SEM (Supporting Information, Figure S8). As observed, many independent urchinlike and flowerlike $NiCo_2O_4$ HSs are mixed together on the nickel foam (Supporting Information, Figure S8a). The first layer on the Ni foam surface is a bed of nanosheet arrays (Supporting Information, Figure S8b). The close-ups of the separate urchinlike and flowerlike $NiCo_2O_4$ HSs are shown in the Supporting Information (Figure S8c,d), suggesting no integration between the nanosheets and nanowires in an order-transposed, two-step hydrothermal process. Given the discussion above, the two-step hydrothermal strategy, in which the low-dimensional NSs growth phase precedes that of the high-dimensional NSs, is an important aspect of the crystal growth process for the $NiCo_2O_4$ MHS.

Figure 4a shows the N_2 adsorption−desorption isotherms of the as-made $NiCo_2O_4$ samples. All of the curves exhibit type IV isotherms with hysteresis loops of different sizes (Figure 4a), which reflects the propensity of mesoporous material to facilitate capillary condensation during the desorption process. The BET surface area of the $NiCo_2O_4$ MHS is calculated to be the highest (104.8, 118.3, and 42.4 $m^2\ g^{-1}$ for NCO1, NCO2, and NCO3, respectively). Figure 4b shows the corresponding pore size distribution which is calculated from the BJH method using the desorption branch of the nitrogen isotherm. The samples NCO2 and NCO3, which incorporate both nanowires and nanosheets, have greater mesoporosity, with wider pore size distribution compared with the nanowire arrays (NCO1). The mesopore sizes of NCO2 and NCO3 have two main centered domains at 2−4 and 11−13 nm. However, the pore volume of NCO2 is significantly higher than that of NCO3, which is consistent with the BET surface area. These results indicate that the MHSs could both obtain a developed mesoporous structure by introducing the nanosheets and achieve a relatively higher specific area in an ordered assembly. Furthermore, the appealing textural properties may not only

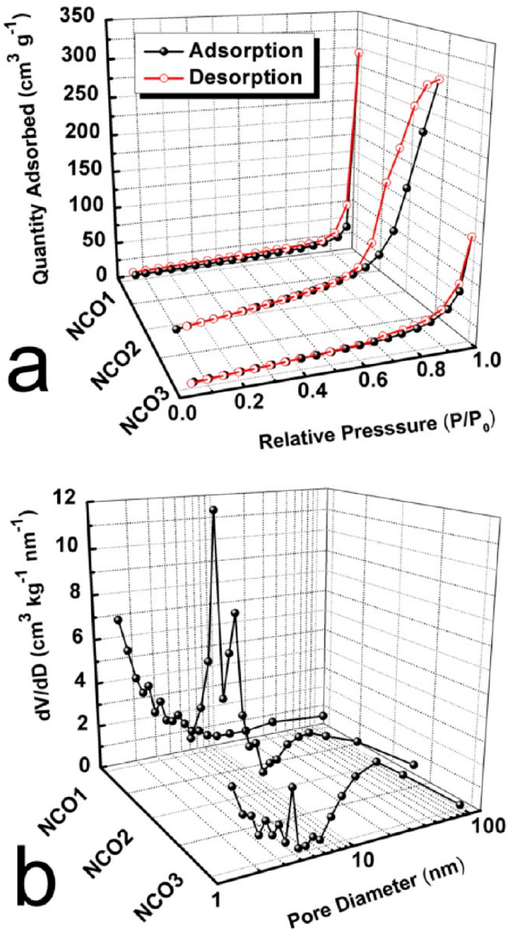

Figure 4. (a) Nitrogen adsorption−desorption isotherms and (b) corresponding pore size distribution curves of as-prepared samples.

permit easy ion access of the electrode/electrolyte interface but also ensure a high electroactive surface area for redox reactions.[23,30]

EIS measurements were carried out to elucidate the effect of the pore architecture and morphology of the mesoporous $NiCo_2O_4$ MHS on electrochemical performance. Figure 5 presents the Nyquist and Bode plots of the three samples after the 20th cycle. The measured impedance spectra were fitted using an equivalent circuit (Figure 5d), which consisted of a bulk solution resistance R_s, charge-transfer resistance R_{ct}, constant phase angle element Q (or CPE), pseudocapacitive element C_{ps} from the redox process, and W (Warburg impedance). As observed in Figure 5a−c, the fit matches the EIS data very well. In the high-frequency region, the $NiCo_2O_4$ MHS shows a much more inconspicuous loop from an expanded view (in the upper part of Figure 5a−c), which indicates the minimal charge-transfer resistance between the electroactive material and the electrolyte interface. Charge-transfer resistance is generally related to the electroactive surface area (a combination of the specific surface area and electrical conductivity) of the electrode materials. The electroactive surface area increased with increasing specific surface area and electrical conductivity. A larger electroactive surface area indicates a lower charge-transfer resistance.[31,32] The lowest calculated value of R_{ct} (0.4901, 0.0364, and 0.9624 Ω for NCO1, NCO2, and NCO3, respectively) corresponds to the largest electroactive surface area of NCO2 because all of the samples share the outstanding electronic conductivity of $NiCo_2O_4$. The rapid transition from the loop to the near-vertical line in the Nyquist plots at low frequencies indicates the low ion diffusive resistance within the mesoporous materials. It is generally recognized that these larger mesopores are always more conducive to transport and diffusion processes. However, NCO1 has the lowest Warburg impedance (0.3567 Ω), followed by NCO2 (0.5144 Ω), with the highest for NCO3 (0.8838 Ω). This result can be explained by the following: (i) the nanosheets' larger mesopores provide a bigger volume for free ion transport,[17] while (ii) the smaller nanowire mesopores have a strong electrolyte wettability and short path length, which are more favorable for the electrolyte permeation and diffusion,[18,33] and, last, (iii) the MHSs assembled, rather than mixed, by the two NSs well balance the advantages of both and obtain a moderate Warburg impedance. Furthermore, this complementary micromechanism of ionic transport based on the pore architecture makes more OH^- reach the large surface of the MHS for electron transfer, allowing the facile interconversion of $O_2^- \leftrightarrow OH^-$ and thereby ensuring the highest electroactive surface area.[4]

The dependences of the real (C') and imaginary (C'') components of capacitance on the operating frequency are shown in Figure 5e,f. The capacitance (C') increased with decreasing frequency in the low-frequency region (Figure 5e). The sharp decrease of capacitance is ascribed to the poor accessibility of electrolyte ions within the deeper pores of the NSs at high frequencies.[34] NCO2 exhibited a much higher capacitance than did the others across the full frequency range of 0.01−1 Hz because the vast electroactive surface area enables much more involvement of the electrode materials in the Faraday reactions. The sharp peak in the graph of the frequency-dependent imaginary component of capacitance (C'') conveys a maximum capacitance (C'') at a frequency f_m (Figure 5f), which corresponds to the relaxation time constant $\tau = 1/f_m$ (inset in Figure 5f).[35] A lower value of τ always indicates faster access of the exposed surface of the electrode.[34,36] Similar to W, a middling numerical value of τ also emphasizes the significant contribution of the nanowires, which vastly accelerate the permeation of the ions. Overall, the MHSs are endowed with both a high electroactive surface area and beneficial pore architecture. This distinctive pore architecture may be particularly useful in preserving the smooth flow of ions at high rates through channels while also alleviating the structural damage caused by volume expansion during high-rate charge−discharge or cycling processes.

To study the applicability of the $NiCo_2O_4$ MHS in supercapacitors, we investigated and compared the capacitive properties of NCO1, NCO2, and NCO3. Figure 6a shows the cyclic voltammetric (CV) curves of the three samples and that of a pure nickel foam electrode at a scan rate of 10 mV s^{-1}. With two typical redox peaks in a potential window of 0−0.5 V, the shapes of all of the curves indicate pseudocapacitive characteristics. However, the intensity of the redox couple attributed to the reversible reaction of Ni(II)/Ni(III) on the nickel surface is much smaller than that of the $NiCo_2O_4$-based electrodes, indicating that the Ni foam contributes little to the total capacitance of the electrodes. Due to the difference in electrode polarization behavior, which is closely related to the physical morphology of the electrode material, there are visible variations in the redox peak positions of the CV curves for the three samples.[37,38] The two typical redox peaks are mainly attributed to the Faradaic redox reactions related to M−O/M−

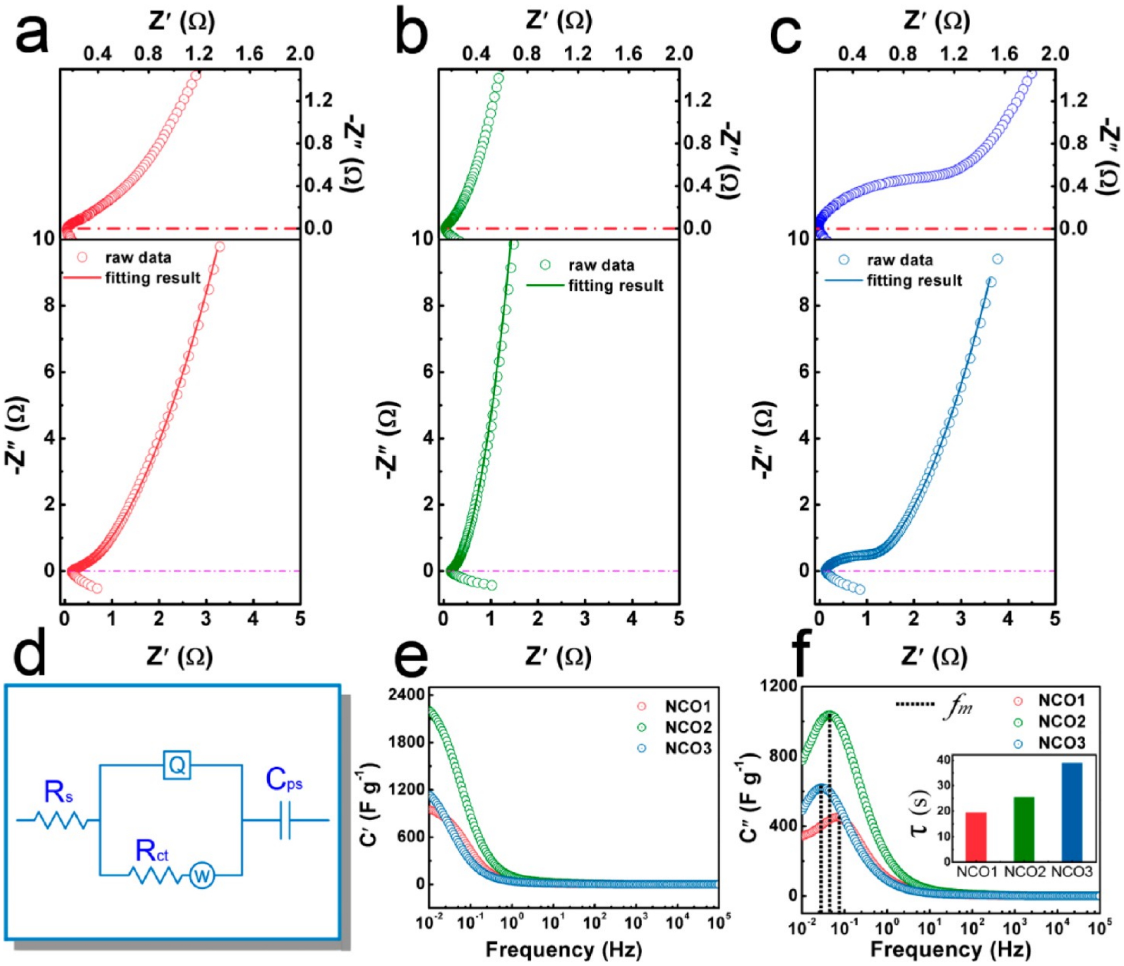

Figure 5. Nyquist plots of (a) NCO1, (b) NCO2, and (c) NCO3 with the imaginary part (*Y*-axis) vs the real part (*X*-axis) of impedance from EIS studies (expanded views of the high frequency region displayed in the upper part). (d) Electrical equivalent circuit used for fitting impedance spectra. Bode plots of (e) real and (f) imaginary parts of specific capacitance for the as-prepared samples (inset, relaxation time constant τ for as-prepared samples).

O−OH (where M represents Ni or Co).[37] The reversible reactions in the alkaline electrolyte are given in eqs 6 and 7.

$$NiCo_2O_4 + OH^- + H_2O \leftrightarrow NiOOH + 2CoOOH + e^- \tag{6}$$

$$CoOOH + OH^- \leftrightarrow CoO_2 + H_2O + e^- \tag{7}$$

Among the three electrodes, NCO2 has shown the largest current response as well as the largest integral area of the CV curve, indicating the largest pseudocapacitance. The CVs of the pure nickel foam electrode and the three samples were also studied at scan rates ranging from 1 to 40 mV s^{-1} (Supporting Information, Figure S9). The current responses increase with the increasing scan rates, and the shapes of the CV curves remain basically unchanged. To quantitatively evaluate and compare the electrochemical performance of the three samples, the specific capacitance (C_{sp}) is calculated from the CV measurements using the following equation:[23,39]

$$C_{sp} = \frac{1}{m\nu(V_f - V_i)} \int_{V_i}^{V_f} I(V)\,dV \tag{8}$$

where C_{sp} is the specific capacitance (F g^{-1}), m is the mass of the active electrode material (g), ν is the potential scan rate (mV s^{-1}), V_f and V_i are the integration limits of the voltammetric curve (V), and $I(V)$ denotes the response current (mA). The corresponding values are shown in Figure 6b. The $NiCo_2O_4$ MHS exhibits the highest value of C_{sp} at varied scan rates, and NCO3 has the lowest. In particular, the specific capacitances of 1518.9, 2368.1, and 1071.3 F g^{-1} are obtained at a scan rate of 10 mV s^{-1} for NCO1, NCO2, and NCO3, respectively. In addition, the area capacitance of the pure nickel foam electrode and those of the three samples were calculated using a variation of eq 8 in which m is replaced by the area of the electrode. Table S1 in the Supporting Information quantifies the contribution of the nickel foam to the area capacitance, which can also be considered negligible.

Further investigation of the capacitive property was conducted using galvanostatic charge−discharge (CD) measurements (Figure 6c and Figure S10 in the Supporting Information). Each of the CD curves has two voltage plateaus that precisely agree with the two typical redox peaks in CV curves within the potential window of 0−0.5 V. The discharge time decreased with increasing current density (Supporting Information, Figure S10). This can be attributed to the increasingly fast electronic and ionic transport rates, which reduce the effective interaction between the ions and the electrode and thereby lead to the attenuation of capacitance. Numerical calculations of the specific capacitance (C) during the galvanostatic charge−discharge processes are based on the following equation:[40]

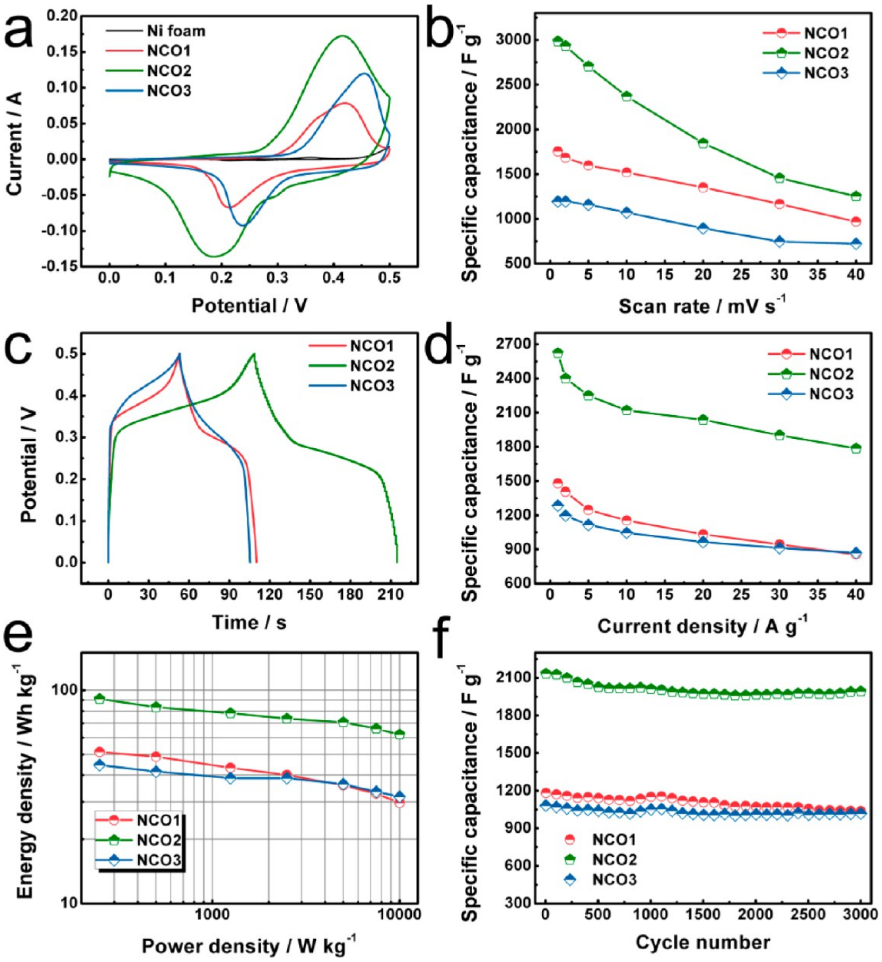

Figure 6. Electrochemical performances of the as-prepared samples: (a) CV curves (after 10 cycles) of the three samples at a scan rate of 10 mV s^{-1}; (b) specific capacitance derived from the CV measurements at scan rates of 1, 2, 5, 10, 20, 30, and 40 mV s^{-1}; (c) CD curves (after 10 cycles) of the three samples at a current density of 10 A g^{-1}; (d) specific capacitance derived from the discharge curves at current densities of 1, 2, 5, 10, 20, 30, and 40 A g^{-1}; (e) Ragone plot of the estimated energy density and power density at various charge−discharge rates; and (f) cycling performance of the three samples measured at a current density of 10 A g^{-1}.

$$C = \frac{I\Delta t}{m\Delta V} \tag{9}$$

where C is the specific capacitance (F g^{-1}), I represents the discharge current (A), and m, ΔV, and Δt designate the mass of active materials (g), potential drop (V) during discharge, and total discharge time (s), respectively. Consistent with the CV results, the $NiCo_2O_4$ MHS displays highest specific capacitance. To illustrate, at a current density of 10 A g^{-1} (Figure 6c), the three samples deliver capacitances of 1154.3, 2121.3, and 1045.8 F g^{-1} for NCO1, NCO2, and NCO3, respectively. The rate performance, which directly depends on the attenuation of capacitance observed in CD measurements, is reflected in Figure 6d. The specific capacitance of the $NiCo_2O_4$ MHS is calculated to be 2623.3 F g^{-1} at a current density of 1 A g^{-1}. However, the value is much smaller for NCO1 and NCO3 (1479.7 and 1285.1 F g^{-1}, respectively). It is worthwhile to note that the specific capacitance of NCO2 is 2037.8 F g^{-1} at a high current density of 20 A g^{-1}, which is ∼78% of that at 1 A g^{-1}. For NCO1 and NCO3, the corresponding values are only 1031.6 and 964 F g^{-1} at 20 A g^{-1}, and the capacitance retentions are 70 and 75%, respectively. Furthermore, NOC2 can still retain 1785.5 F g^{-1} specific capacitance (∼68% retention), even at a current density as high as 40 A g^{-1}. Comparable values at the same current density are 854.7 F g^{-1} (∼58% retention) for NCO1 and 868.2 F g^{-1} (∼68% retention) for NCO3.

In view of the high capacitance and excellent rate capability, we further investigated the indicators of energy density (E) and power density (P), which are calculated from the discharge curves according to eqs 10 and 11.

$$E = \frac{1}{7.2}C(\Delta V)^2 \tag{10}$$

$$P = 3600\frac{E}{\Delta t} \tag{11}$$

where E is the specific energy density (Wh kg^{-1}), C refers to the specific capacitance (F g^{-1}) derived from CD measurements, ΔV is the potential drop (V) during discharge, P represents the power density (W kg^{-1}), and Δt is the duration for a full discharge (s). The Ragone plots based on the calculation are presented in Figure 6e. As observed, the energy density of NCO2 steadily decreases from 91.1 to 62 Wh kg^{-1}, with increasing power density from 250 to 10 000 W kg^{-1}. In contrast, the other two samples exhibit much lower energy density (51.4−29.7 and 44.6−31.7 Wh kg^{-1} for NCO1 and NCO2, respectively) as the discharge current increases from 1 to 40 A g^{-1}. Thus, the $NiCo_2O_4$ MHS can deliver an ultrahigh energy density while maintaining its inherently high power output, suggesting great potential as an electrode material for use in supercapacitors. To examine the electrode persistence and stability when working at high rates, we investigated the cycle performance of the $NiCo_2O_4$ MHS through CD measurements at a 10 A g^{-1} current density for 3000 cycles (Figure 6f). During the course of prolonged cycling, we record 1 of every 100 cycles, with the fourth cycle as the first point. As depicted, the fourth, 1504th, and 3000th cycles show the explicit differences caused by the gradual decrease in capacitance with cycling (Supporting Information, Figure S11). After 1500 cycles, the specific capacitance remains nearly unchanged. Values calculated from discharge curves show approximately 12.2, 6.6, and 5.9% losses in specific capacitance after 3000 cycles for NCO1, NCO2, and NCO3, respectively. This slow deterioration, together with the high specific capacitance (2133.4, 1983.9, and 1993 F g^{-1} for the fourth, 1504th, and 3000th cycles, respectively) at a high rate, reveals the excellent cycling performance of NCO2. After charging−discharging for 3000 cycles, the morphology and structure of the MHSs can be largely retained with only slight aggregation observed (Supporting Information, Figure S12). Moreover, with the exception of NCO3, no peeling of the $NiCo_2O_4$ sample from the electrode surface was observed after the long-term cycling (Supporting Information, Figure S13). The observed peeling may be attributed to the failed integration of the nanowires and nanosheets in the order-transposed hydrothermal growth. As a result, those independent HSs cannot provide good mechanical adhesion with each other.

The above electrochemical measurements demonstrate that the $NiCo_2O_4$ MHS embodies a major improvement on the electrochemical performance of nickel−cobalt oxide, which is remarkably comparable with previously reported studies of $NiCo_2O_4$ MSs/NSs (Supporting Information, Table S2). These prominent enhancements radically consist of the groundbreaking integration of 1D and 2D NSs, in which both could boost the capacitive property via two-way promotion and interaction. Foremost, the high specific surface area of nanosheets encircled by nanowires, resulting from an ordered assembly, could expose as many electrode materials for the faradic reaction as possible. The relatively large open spaces between nanosheets provide a huge volume for permeation and storage of electrolyte in the 3D architectures. At the same time, the low-dimensional nanowires, with their correspondingly smaller mesopores, further facilitate the permeation and diffusion of the ions, fully wetting the exposed surface of electrode materials. Not only will this ensure abundant electroactive sites for redox reactions and, consequently, a higher specific capacitance, but it will also guarantee the excellent rate and cycling performance of the $NiCo_2O_4$ MHS due to the arresting pore architectures and the complementary micromechanism of ionic transport. Moreover, this simple binder-free electrode system, based on an in situ growth and tableting processing, might be more practical in high performance supercapacitors. Taken individually, these MHSs may serve as independent "workshops", which efficiently contribute to the total electrochemical performance. Conversely, these MHSs are also closely associated with each other, easily transporting electrons from the substrate and forming a powerful conductive network, thereby promoting the efficient functioning of these "workshops".

4. CONCLUSION

In summary, we have successfully synthesized $NiCo_2O_4$ MHSs consisting of 1D nanowires and 2D nanosheets on nickel foam via a simple and controlled hydrothermal method. The low-dimensional nanowire is found to hold priority in the growth order, rather than the high-dimensional nanosheet, for the effective integration of these different NSs into the $NiCo_2O_4$ MHS assembly. It is found that the $NiCo_2O_4$ MHS shows superior specific capacitances of 2623.3 and 1785.5 F g^{-1} under current densities of 1 and 40 A g^{-1}, respectively, with an excellent cycling stability (only 6.6% loss after 3000 cycles). The remarkable electrochemical performance is likely due to the vast electroactive surface area and favorable mesoporous architecture, formed in the integrated assemblies. Furthermore, these results demonstrate the importance of this original design for advanced electrode materials with improved performance for energy storage applications, which is achievable via simple and flexible methods.

■ ASSOCIATED CONTENT

Ⓢ Supporting Information

EDX patterns of the samples. Supplementary SEM images of the samples. Supplementary data of electrochemical performance. Comparison of electrochemical performance of $NiCo_2O_4$ MHSs with some previously reported $NiCo_2O_4$ MSs/NSs. This material is available free of charge via the Internet at http://pubs.acs.org.

■ AUTHOR INFORMATION

Corresponding Authors

*E-mail: yf_gao@imut.edu.cn.
*E-mail: liyueming@ysu.edu.cn.

Notes

The authors declare no competing financial interest.

■ ACKNOWLEDGMENTS

This work was financially supported by the National Natural Science Foundation of China (No. 21266018), science and technology projects of the Science and Technology Department of Inner Mongolia Autonomous Region, People's Republic of China (No. 20110401 and No. 20130409), the Natural Science Foundation of Inner Mongolia, People's Republic of China (No. 2010MS0218), and the Scientific Research Foundation for the Returned Overseas Chinese Scholars State Education Ministry.

■ REFERENCES

(1) Winter, M.; Brodd, R. J. What Are Batteries, Fuel Cells, and Supercapacitors? *Chem. Rev.* **2004**, *104*, 4245−4270.

(2) Simon, P.; Gogotsi, Y. Materials for Electrochemical Capacitors. *Nat. Mater.* **2008**, *7*, 845−854.

(3) Chen, P.-C.; Shen, G.; Shi, Y.; Chen, H.; Zhou, C. Preparation and Characterization of Flexible Asymmetric Supercapacitors Based on Transition-Metal-Oxide Nanowire/Single-Walled Carbon Nanotube Hybrid Thin-Film Electrodes. *ACS Nano* **2010**, *4*, 4403−4411.

(4) Wang, G.; Zhang, L.; Zhang, J. A Review of Electrode Materials for Electrochemical Supercapacitors. *Chem. Soc. Rev.* **2012**, *41*, 797−828.

(5) Zhang, Q.; Uchaker, E.; Candelaria, S. L.; Cao, G. Nanomaterials for Energy Conversion and Storage. *Chem. Soc. Rev.* **2013**, *42*, 3127−3171.

(6) Li, H. B.; Yu, M. H.; Wang, F. X.; Liu, P.; Liang, Y.; Xiao, J.; Wang, C. X.; Tong, Y. X.; Yang, G. W. Amorphous Nickel Hydroxide

Nanospheres with Ultrahigh Capacitance and Energy Density as Electrochemical Pseudocapacitor Materials. *Nat. Commun.* **2013**, *4*, 1894.

(7) Lu, Q.; Chen, J. G.; Xiao, J. Q. Nanostructured Electrodes for High-Performance Pseudocapacitors. *Angew. Chem., Int. Ed.* **2013**, *52*, 1882−1889.

(8) Wu, C.; Lu, X.; Peng, L.; Xu, K.; Peng, X.; Huang, J.; Yu, G.; Xie, Y. Two-dimensional Vanadyl Phosphate Ultrathin Nanosheets for High Energy Density and Flexible Pseudocapacitors. *Nat. Commun.* **2013**, *4*, 2431.

(9) Zhao, X.; Sanchez, B. M.; Dobson, P. J.; Grant, P. S. The Role of Nanomaterials in Redox-based Supercapacitors for Next Generation Energy Storage Devices. *Nanoscale* **2011**, *3*, 839−855.

(10) Xing, Z.; Chu, Q.; Ren, X.; Ge, C.; Qusti, A. H.; Asiri, A. M.; Al-Youbi, A. O.; Sun, X. Ni_3S_2 Coated ZnO Array for High-performance Supercapacitors. *J. Power Sources* **2014**, *245*, 463−467.

(11) Yang, J.; Duan, X.; Qin, Q.; Zheng, W. Solvothermal Synthesis of Hierarchical Flower-like β-NiS with Excellent Electrochemical Performance for Supercapacitors. *J. Mater. Chem. A* **2013**, *1*, 7880−7884.

(12) Tiwari, J. N.; Tiwari, R. N.; Kim, K. S. Zero-dimensional, One-dimensional, Two-dimensional and Three-dimensional Nanostructured Materials for Advanced Electrochemical Energy Devices. *Prog. Mater. Sci.* **2012**, *57*, 724−803.

(13) Hou, Y.; Cheng, Y.; Hobson, T.; Liu, J. Design and Synthesis of Hierarchical MnO_2 Nanospheres/Carbon Nanotubes/Conducting Polymer Ternary Composite for High Performance Electrochemical Electrodes. *Nano Lett.* **2010**, *10*, 2727−2733.

(14) Taberna, P. L.; Mitra, S.; Poizot, P.; Simon, P.; Tarascon, J. M. High Rate Capabilities Fe_3O_4-based Cu Nano-architectured Electrodes for Lithium-ion Battery Applications. *Nat. Mater.* **2006**, *5*, 567−573.

(15) Wei, T.-Y.; Chen, C.-H.; Chien, H.-C.; Lu, S.-Y.; Hu, C.-C. A Cost-Effective Supercapacitor Material of Ultrahigh Specific Capacitances: Spinel Nickel Cobaltite Aerogels from an Epoxide-Driven Sol-Gel Process. *Adv. Mater.* **2010**, *22*, 347−351.

(16) Yu, L.; Wu, H.; Wu, T.; Yuan, C. Morphology-controlled Fabrication of Hierarchical Mesoporous $NiCo_2O_4$ Micro-/nanostructures and Their Intriguing Application in Electrochemical Capacitors. *RSC Adv.* **2013**, *3*, 23709−23714.

(17) Yuan, C.; Li, J.; Hou, L.; Zhang, X.; Shen, L.; Lou, X. W. Ultrathin Mesoporous $NiCo_2O_4$ Nanosheets Supported on Ni Foam as Advanced Electrodes for Supercapacitors. *Adv. Funct. Mater.* **2012**, *22*, 4592−4597.

(18) Jiang, H.; Ma, J.; Li, C. Hierarchical porous $NiCo_2O_4$ nanowires for high-rate supercapacitors. *Chem. Commun.* **2012**, *48*, 4465−4467.

(19) Zhang, G. Q.; Wu, H. B.; Hoster, H. E.; Chan-Park, M. B.; Lou, X. W. Single-crystalline $NiCo_2O_4$ Nanoneedle Arrays Grown on Conductive Substrates as Binder-free Electrodes for High-performance Supercapacitors. *Energy Environ. Sci.* **2012**, *5*, 9453−9456.

(20) Du, J.; Zhou, G.; Zhang, H.; Cheng, C.; Ma, J.; Wei, W.; Chen, L.; Wang, T. Ultrathin Porous $NiCo_2O_4$ Nanosheet Arrays on Flexible Carbon Fabric for High-Performance Supercapacitors. *ACS Appl. Mater. Interfaces* **2013**, *5*, 7405−7409.

(21) Wang, Q.; Liu, B.; Wang, X.; Ran, S.; Wang, L.; Chen, D.; Shen, G. Morphology Evolution of Urchin-like $NiCo_2O_4$ Nanostructures and Their Applications as Psuedocapacitors and Photoelectrochemical Cells. *J. Mater. Chem.* **2012**, *22*, 21647−21653.

(22) Liu, X. Y.; Zhang, Y. Q.; Xia, X. H.; Shi, S. J.; Lu, Y.; Wang, X. L.; Gu, C. D.; Tu, J. P. Self-assembled Porous $NiCo_2O_4$ Heterostructure Array for Electrochemical Capacitor. *J. Power Sources* **2013**, *239*, 157−163.

(23) Wu, H. B.; Pang, H.; Lou, X. W. Facile Synthesis of Mesoporous $Ni_{0.3}Co_{2.7}O_4$ Hierarchical Structures for High-performance Supercapacitors. *Energy Environ. Sci.* **2013**, *6*, 3619−3626.

(24) Li, L.; Cheah, Y.; Ko, Y.; Teh, P.; Wee, G.; Wong, C.; Peng, S.; Srinivasan, M. The Facile Synthesis of Hierarchical Porous Flower-like $NiCo_2O_4$ with Superior Lithium Storage Properties. *J. Mater. Chem. A* **2013**, *1*, 10935−10941.

(25) Xiao, J.; Yang, S. Sequential Crystallization of Sea Urchin-like Bimetallic (Ni, Co) Carbonate Hydroxide and Its Morphology Conserved Conversion to Porous $NiCo_2O_4$ Spinel for Pseudocapacitors. *RSC Adv.* **2011**, *1*, 588−595.

(26) Chen, H.; Jiang, J.; Zhang, L.; Qi, T.; Xia, D.; Wan, H. Facilely Synthesized Porous $NiCo_2O_4$ Flowerlike Nanostructure for High-rate Supercapacitors. *J. Power Sources* **2014**, *248*, 28−36.

(27) Hu, C.-C.; Wang, C.-C. Improving the Utilization of Ruthenium Oxide within Thick Carbon-ruthenium Oxide Composites by Annealing and Anodizing for Electrochemical Supercapacitors. *Electrochem. Commun.* **2002**, *4*, 554−559.

(28) Chen, W.-C.; Hu, C.-C.; Wang, C.-C.; Min, C.-K. Electrochemical Characterization of Activated Carbon-ruthenium Oxide Nanoparticles Composites for Supercapacitors. *J. Power Sources* **2004**, *125*, 292−298.

(29) Vereda, F.; Rodríguez-González, B.; de Vicente, J.; Hidalgo-Álvarez, R. Evidence of Direct Crystal Growth and Presence of Hollow Microspheres in Magnetite Particles Prepared by Oxidation of $Fe(OH)_2$. *J. Colloid Interface Sci.* **2008**, *318*, 520−524.

(30) Wang, H.; Gao, Q.; Jiang, L. Facile Approach to Prepare Nickel Cobaltite Nanowire Materials for Supercapacitors. *Small* **2011**, *7*, 2454−2459.

(31) Wu, M.-S.; Hsieh, H.-H. Nickel Oxide/Hydroxide Nanoplatelets Synthesized by Chemical Precipitation for Electrochemical Capacitors. *Electrochim. Acta* **2008**, *53*, 3427−3435.

(32) Meher, S. K.; Rao, G. R. Ultralayered Co_3O_4 for High-Performance Supercapacitor Applications. *J. Phys. Chem. C* **2011**, *115*, 15646−15654.

(33) Han, D.; Xu, P.; Jing, X.; Wang, J.; Yang, P.; Shen, Q.; Liu, J.; Song, D.; Gao, Z.; Zhang, M. Trisodium Citrate Assisted Synthesis of Hierarchical NiO Nanospheres with Improved Supercapacitor Performance. *J. Power Sources* **2013**, *235*, 45−53.

(34) Biswal, M.; Banerjee, A.; Deo, M.; Ogale, S. From Dead Leaves to High Energy Density Supercapacitors. *Energy Environ. Sci.* **2013**, *6*, 1249−1259.

(35) Xiang, C.; Li, M.; Zhi, M.; Manivannan, A.; Wu, N. A Reduced Graphene Oxide/Co_3O_4 Composite for Supercapacitor Electrode. *J. Power Sources* **2013**, *226*, 65−70.

(36) Yan, J.; Sun, W.; Wei, T.; Zhang, Q.; Fan, Z.; Wei, F. Fabrication and Electrochemical Performances of Hierarchical Porous $Ni(OH)_2$ Nanoflakes Anchored on Graphene Sheets. *J. Mater. Chem.* **2012**, *22*, 11494−11502.

(37) Wang, X.; Han, X.; Lim, M.; Singh, N.; Gan, C. L.; Jan, M.; Lee, P. S. Nickel Cobalt Oxide-Single Wall Carbon Nanotube Composite Material for Superior Cycling Stability and High-Performance Supercapacitor Application. *J. Phys. Chem. C* **2012**, *116*, 12448−12454.

(38) Chen, Y.; Qu, B.; Hu, L.; Xu, Z.; Li, Q.; Wang, T. High-performance Supercapacitor and Lithium-ion Battery Based on 3D Hierarchical NH_4F-induced Nickel Cobaltate Nanosheet-nanowire Cluster Arrays as Self-supported Electrodes. *Nanoscale* **2013**, *5*, 9812−9820.

(39) Salunkhe, R. R.; Jang, K.; Lee, S.-w.; Ahn, H. Aligned Nickel-cobalt Hydroxide Nanorod Arrays for Electrochemical Pseudocapacitor Applications. *RSC Adv.* **2012**, *2*, 3190−3193.

(40) Singh, A. K.; Sarkar, D.; Khan, G. G.; Mandal, K. Unique Hydrogenated Ni/NiO Core/Shell 1D Nano-heterostructures with Superior Electrochemical Performance as Supercapacitors. *J. Mater. Chem. A* **2013**, *1*, 12759−12767.